KNOW-BLADE task-4 report: Navier-Stokes aeroelasticity

Politis, E.S.; Nikolaou, I.G.; Chaviaropoulos, P.K.; Bertagnolio, F.; Sørensen, Niels N.; Johansen, Jeppe

Publication date:
2004

Document Version
Publisher's PDF, also known as Version of record

RISØ

Risø-R-1492(EN)

KNOW-BLADE Task-4 report; Navier-Stokes Aeroelasticity

E.S. Politis*, I.G. Nikolaou*, P.K. Chaviaropoulos*,

F. Bertagnolio¤, N.N. Sørensen¤ and J. Johansen¤

* Center for Renewable Energy Sources, CRES, EL-19009 Pikermi Attiki, Greece
¤ Wind Energy Department, Risø National Laboratory, DK-4000 Roskilde, Denmark

Risø National Laboratory
Roskilde
Denmark
January 2005

Author: E.S. Politis, I.G. Nikolaou, P.K. Chaviaropoulos, F. Bertagnolio, N.N. Sørensen and J. Johansen
Title: KNOW-BLADE Task-4 report; Navier-Stokes Aeroelasticity
Department: Wind Energy Department

Risø-R-1492(EN)
January 2005

Abstract (max. 2000 char.):

The problem of the aeroelastic stability of wind turbine blades is addressed in this report by advancing the aerodynamic modelling in the beam element type codes from the engineering-type empirical models to unsteady, 2D or 3D, Navier-Stokes solvers. In this project, structural models for the full wind turbine blade have been combined with 2D and 3D unsteady Navier-Stokes solvers. The relative disadvantage of the quasi-3D approach (where the elastic solver is coupled with a 2D Navier-Stokes solver) is its inability to model induced flow. The lack of a validation test case did not allow for quantitative comparisons with experimental data to be carried out; instead the results of the advanced aeroelastic tools are qualitatively cross-compared.

All investigated methods predicted qualitatively similar results. They all resulted in positive aerodynamic damping values for the flap mode, in a decrease in damping with the increase of wind speeds and in a minimum value for the damping for wind speed around 15~m/s. The eigenvalue analyses resulted in steeper distributions for this mode. The agreement in aerodynamic damping decrease with the increase of wind speed is also observed in the distributions for the lead-lag mode.
In perspective, the uncoupled, linear method results in higher values of aerodynamic damping compared to the 3D aeroelastic tool. The quasi-3D tool results in lower aerodynamic damping values in the higher wind speeds and in lower damping values in the lower wind speed regime.

Apart from the computations for the full blade, 2D computations for the so-called “typical section” have been carried out. The 2D aeroelastic tools resulted in similar aerodynamic damping values. Qualitative agreement was better for the lead-lag mode. The presence of roughness tapes has a small, rather negligible impact on aeroelastic stability as depicted by the results of both aeroelastic tools. On the other hand, in conformity to the inability of the adopted computational model to successfully predict the corresponding test cases under work package 2 of the project, the aeroelastic tools are not capable to predict the correct physical trends when the blade is equipped with stall strips. The resulting decrease in damping in the computations by both tools is not in accordance with experience.

ISSN 0106-2840
ISBN 87-550-3395-4

Contract no.:
ENK6-CT-2001-00503

Group's own reg. no.:
1110033-00

Sponsorship:

Cover :

Pages: 32
Tables: 3
References: 28

Risø National Laboratory
Information Service Department
P.O.Box 49
DK-4000 Roskilde
Denmark
Telephone +45 46774004
bibl@risoe.dk
Fax +45 46774013
www.risoe.dk

CENTRE FOR RENEWABLE
ENERGY SOURCES
C.R.E.S.

KNOW–BLADE Task–4:
Navier–Stokes Aeroelasticity

October 2004

Technical Report

19th km Marathonos Ave, GR–19009, Pikermi, Attiki
Tel.: (+30) 210–660–33–00, Fax: (+30) 210–660–33–01

Wind Turbine Blade Aerodynamics and Aeroelasticity: Closing Knowledge Gaps (KNOW–BLADE)

Contract No: ENK6–CT–2001–00503

Technical Report on Work Package 4: "Navier–Stokes Aeroelasticity"

Edited by: E. S. Politis (CRES)

Contributed by:

- F. Bertagnolio, N. N. Sørensen & J. Johansen (Risø)
- E. S. Politis, I. G. Nikolaou & P. K. Chaviaropoulos (CRES)

- Final Version: October 2004

Contents

Chapter 1

Introduction

This report deals with the advanced aeroelastic stability tools for wind turbine blades, based on Navier–Stokes solvers, developed by two partners under work package 4 of the project "**Wind Turbine Blade Aerodynamics & Aeroelasticity: Closing Knowledge Gaps**" (KNOW–BLADE) partially funded by the European Commission under the contract ENK6–CT–2001–00503. The two partners are the *Risø National Laboratory* (RISØ, DK) and the *Centre for Renewable Energy Sources* (CRES, EL). The latter institute is the leader of the work package 4.

The overall objectives of KNOW–BLADE project are to advance and develop a series of tools based on existing Navier–Stokes solvers, dealing with a number of problems connected to wind turbine blade design. The ultimate goal is to allow the wind turbine industry to design and manufacture optimal, customised blades in reduced cost and shorter time-to-market.

Wind industry community shows an increasing interest in the aeroelastic stability of large wind turbine blades. This interest is mainly caused by the current design trends towards lighter blades of increased ratios of aerodynamic loads to inertia. The key parameter for reliable prediction of the aeroelastic simulation and stability is the description of the aerodynamic loads. Until the present project, aerodynamic modelling was accomplished by means of engineering-type empirical models (as the Onera or the Beddoes–Leishman) with the use of Navier–Stokes solvers being restricted only in a two-dimensional basis, to aeroelastic tools developed for the so-called "typical section". So, the specific objectives of this work package are:

- To advance the state of the art Navier–Stokes aeroelasticity tools from two-dimensional to quasi-three-dimensional and fully three-dimensional codes, making it possible to investigate the damping characteristics of real rotor blades, rather that blade sections.
- In close relation with work package 2, where aerodynamic accessories are modelled by means of Navier–Stokes solvers, to investigate the aeroelastic damping characteristics of aerodynamic accessories on two-dimensional airfoil sections, providing stability information for different configurations.

In this context, the work package 4 comprises the following tasks:

Task 4.1 Quasi-three-dimensional aeroelasticity
Development of a quasi-three-dimensional aeroelastic model based on an existing three-dimensional structural model of the beam element type, and an existing two-dimensional Navier–Stokes solver. The Navier–Stokes solver is applied at a few spanwise sections.

Task 4.2 Fully three-dimensional aeroelasticity
Development of a full three-dimensional-aeroelastic model for the wind turbine blade,

based on existing three-dimensional structural model of the beam element type, and an existing fully three-dimensional Navier–Stokes solver.

Task 4.3 Two-dimensional aeroelastic studies with aerodynamic accessories
Based on existing two-dimensional Navier–Stokes aeroelastic codes, studies of the influence on the stability of several of the aerodynamic accessories from work package 2 are performed.

Quasi-three-dimensional aeroelastic computations have been carried out by CRES, while fully-three-dimensional ones were performed by Risø. Both partners conducted aeroelastic stability studies in the presence of such aerodynamic accessories as stall-strips and roughness tapes.

This is the final technical report and the main deliverable for work package 4 of the KNOW–BLADE project. It is divided in four chapters. In the following chapter all codes used (Navier–Stokes solvers and structural models) are briefly presented. In chapter 3, the test cases defined for both the three-dimensional (fully and quasi) and the two-dimensional analyses are described. In the next chapter, the aerodynamic damping results are plotted and cross-compared. For the full three-dimensional blade, comparisons are presented between the fully three-dimensional simulation and the quasi-three-dimensional simulation, as well as for nonlinear simulations and eigenvalue analyses employing engineering-type models for the aerodynamics. Next, comparisons between fully three-dimensional and two-dimensional simulations are provided aiming at evaluating the latter ones with respect to full three-dimensional computations. Then, the corresponding two-dimensional simulations without aerodynamic accessories by the two partners involved are cross-compared to define a basis according to which the results for the aeroelastic behaviour in the presence of aerodynamic accessories will be judged. Finally, all information gathered from the previous comparisons is evaluated for direct use by the wind energy community.

Chapter 2

Code Descriptions

In this chapter the aeroelastic codes are described. First, brief descriptions of the two Navier–Stokes solvers employed in the computations are provided, followed by descriptions of the elastic solvers for the full three-dimensional blade and the "typical section". Finally, comments about the coupling of the aerodynamic and the elastic solvers are provided.

2.1 The Navier–Stokes Solvers

2.1.1 EllipSys3D Code

The EllipSys3D code has been developed in co-operation between the Department of Mechanical Engineering at DTU and the Department of Wind Energy at Risø National Laboratory, see [1, 2, 3]. It is designed to solve the three-dimensional Navier–Stokes equations for an incompressible fluid. It uses a cell-centered grid arrangement for the pressure field and the Cartesian velocity components. The equations are discretised by means of a finite volume formulation. The well-known velocity-pressure decoupling is circumvented by using the Rhie and Chow interpolation technique [4]. The PISO algorithm is used for solving the momentum and pressure equations in a predictor–corrector fashion [5]. The Second order Upwind Differencing Scheme (SUDS) is applied to compute the convective fluxes [6], whereas viscous terms are discretised with the classical second order central difference scheme. A subiteration technique is implemented in order to increase the critical time step. The fluid flow variables are advanced in time by means of a second order temporal implicit scheme.

Turbulence closure is accomplished by means of the $k-\omega$ SST turbulence model by Menter [7] in its original version. The flow was assumed to be fully turbulent and no transition model was implemented.

The deformation of the blades in the aeroelastic simulations implies a distortion of the computational grid which has to be considered in the numerical scheme. The convective fluxes are then given in Arbitrary Lagrangian–Eulerian form [8] to take into account the local grid velocity. The distortion of the computational grid according to the blades deformation is performed as follows. In the vicinity of the blades, the grid is distorted as an elastic solid body according to the displacement of the blade surface, whereas in the far field the grid is assumed to be fixed. In the intermediate regions between the blades, and between the individual blades and the far field, arithmetic blending functions are used in order to ensure a smooth distorted grid. This strategy has proven to give good results, even in the case of severe deformations of the blades. On the top of the previously described deformation, an overall rotation of the grid is superimposed to conform to the rotor blades rotation.

The numerical code requires that the computational domain must be mapped onto a

boundary-fitted structured grid. In order to facilitate the mapping and to take advantage of the new generation of parallel computers, a domain decomposition technique has been implemented in the numerical code. The meshes of the individual subdomains must be conformal, i.e. the grid lines must match at the interfaces between the subdomains. In a parallel computing platform, each processor is handling a certain number of subdomains. The communication between the several processors is performed by using the MPI-library.

2.1.2 Navier–Stokes Solver of CRES

The Navier–Stokes solver of CRES is based on a finite-volume discretization scheme, where all flow variables are collocated at the cell-centres of the control volumes [9]. Structured grids of any kind can be incorporated in the solution algorithm.

Standard second order accurate discretization schemes are used for the diffusion terms in the momentum conservation equations. At the same time, multiple schemes of varying accuracy are available for the discretization of the convection terms in the same equations; the most commonly used being a second order accurate upwind scheme.

The divergence-free velocity constraint is enforced by means of the SIMPLE method [10]. In the context of it, the mass conservation equation is rewritten as an equation for the pressure correction variable, which updates both the pressure and the velocity field at the final step of any iteration. The odd-even node decoupling which is a common feature of incompressible flow solvers is alleviated by a special disretization of the pressure terms in the pressure correction equation [4]. The numerics of the method feature a multi-grid possibility that is used for enhanced convergence behavior.

Turbulence can be approximated by means of the standard $k-\epsilon$ turbulence model. Other available turbulence models include the $k-\omega$ and the $k-\omega$ SST model [7]; the latter being the one actually employed at all computations reported herein.

2.2 The Elastic Solvers

2.2.1 Elastic Solver for the Full Blade

The structural model employed in this project derives through a finite element formulation based on a 2-node, 12-degree-of-freedom (DOF) beam element [11]. The dynamic equation of motion is expressed for each rotating element using Lagrange formulation. The beam element used is a two-node element with three translation ($u,\ v,\ w$) and three rotation ($\phi_X,\ \phi_Y,\ \phi_Z$) DOFs per node. Here u, v and w are displacements in the x_B (spanwise), y_B (lead–lagwise) and z_B (flapwise) directions, respectively. The corresponding velocities are denoted as $\dot{u},\ \dot{v}$ and $\dot{w}$.

To express the strain energy integrals, the extended displacement vector is suitably parameterized in terms of the generalized coordinates (end-node values), employing linear and cubic interpolation functions.

Introducing the total potential and kinetic energy of the beam elements in the Lagrange's equation and performing the necessary calculus the equation of motion results for a rotating beam element:

$$\mathbf{M}_E\ \ddot{\mathbf{q}}_E + \mathbf{C}_E\ \dot{\mathbf{q}}_E + (\mathbf{K}_E + \mathbf{\Phi}_E)\ \ \mathbf{q}_E = \mathbf{f}_{R_E} \tag{2.1}$$

with the element mass $\mathbf{M}_E$, the generalized Coriolis $\mathbf{C}_E$, the stiffness $\mathbf{K}_E$ and the centrifugal $\mathbf{\Phi}_E$ matrices, as well as the external forces vector $\mathbf{f}_E$ (including both the aerodynamic and

the inertia forces), expressed at the moving-blade system, as

$$\begin{aligned}
\mathbf{M}_E &= \int_0^L \rho A \mathbf{G}^T \mathbf{G} dx + \int_0^L J \mathbf{H}^T \mathbf{H} dx \\
\mathbf{C}_E &= 2 \int_0^L \rho A \mathbf{G}^T \mathbf{T}_B^T \dot{\mathbf{T}}_B \mathbf{G} dx \\
\mathbf{\Phi}_E &= \int_0^L \rho A \mathbf{G}^T \mathbf{T}_B^T \ddot{\mathbf{T}}_B \mathbf{G} dx \\
\mathbf{D}_E &= \int_0^L \rho A \mathbf{G}^T \mathbf{T}_B^T \ddot{\mathbf{T}}_A dx
\end{aligned}$$

Subscript E denotes element properties, ρ stands for the element density, A for the element cross-section area and J for its polar inertia. $\mathbf{T}_B$ is the rotation matrix from the absolute to the relative, moving with the blade, frame. Over-dots indicate time derivatives. Matrices $\mathbf{G}$ and $\mathbf{H}$ are simple expressions of the interpolation functions that are introduced to interrelate the displacement vector with the end-node values. L stands for the element lenght.

The element matrices are assembled into global mass, damping and stiffness matrices following standard practice. The assembly yields:

$$\mathbf{M}\,\ddot{\mathbf{q}} + \mathbf{C}\,\dot{\mathbf{q}} + \mathbf{K}\,\mathbf{q} = \mathbf{f} \tag{2.2}$$

with $\mathbf{q}$ being the global displacement vector and $\mathbf{f}$ the external force vector, both expressed in the moving frame of reference. The integration of equation (2.2) is performed using the Newmark' s method, which is second order accurate in time.

2.2.2 Elastic Solver for the "Typical Section"

For the typical section the stall-induced flap–lag flutter problem is studied in blade sections with and without aerodynamic accessories. Stall flutter denotes unstable aeroelastic performance at stall conditions. The typical rotating blade section is hinged in such a way that its motion has two independent translational degrees of freedom: a chordwise one (lead–lag), denoted Z; and one perpendicular to that (flap), denoted Y (see Figure 2.1). The inflow conditions are assumed to be steady.

The derivation of the equation of motion of the stall-induced flap–lag flutter model problem is described in detail in [12]. After appropriate manipulation and non-dimensionalization the following expression is obtained

$$\begin{bmatrix} 1 & 0 \\ 0 & 1 \end{bmatrix} \begin{Bmatrix} z'' \\ y'' \end{Bmatrix} + 2\kappa \begin{bmatrix} \xi_z \overline{\omega}_z & 0 \\ 0 & \xi_y \overline{\omega}_y \end{bmatrix} \begin{Bmatrix} z' \\ y' \end{Bmatrix} + \kappa^2 \begin{bmatrix} \overline{\omega}_z^2 + 1 & 0 \\ 0 & \overline{\omega}_y^2 \end{bmatrix} \begin{Bmatrix} z \\ y \end{Bmatrix} = \frac{R_f}{2} \begin{Bmatrix} C_z \\ C_y \end{Bmatrix} \tag{2.3}$$

where the vector of unknowns introduces the normalized (by the airfoil chord) translations z and y, the primes denote differentiation with respect to the reduced time $\tau = (U_\infty/C)t$. The reduced frequency κ is defined as $\kappa = (\Omega C)/U_\infty$ and the ratio of the air density to the linear density of the blade $R_f = (C^2 \rho_\alpha)/\overline{\rho}$. The additional parameters needed to obtain a completely closed aeroelastic system are the structural properties of the hinge, the normalized natural frequencies $\overline{\omega}_i = \omega_i/\Omega$, the damping ratios ξ_i and the force coefficients C_z and C_y along the z and y directions respectively.

The above aeroelastic equation of motion has been coupled with the Navier–Stokes solvers described above.

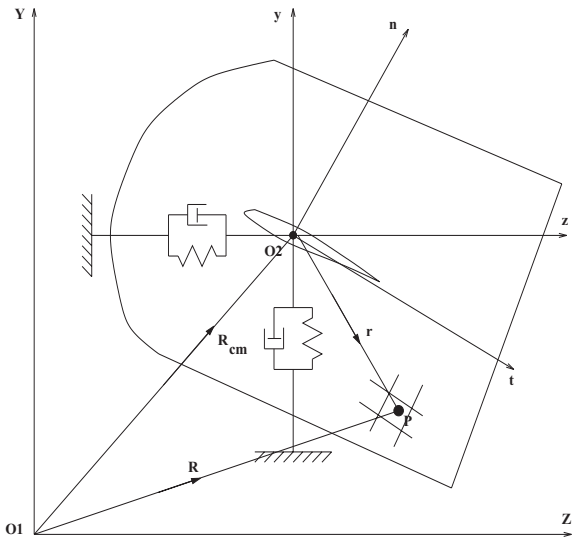

Figure 2.1: Modelling of the two–dimensional aeroelastic problem.

2.3 Modelling of the Aerodynamic Accessories

Both aerodynamic accessories encountered (stall strips and roughness tapes) are modelled by either modifying the Navier–Stokes solvers (the law of the wall in particular for the roughness tapes) or employing a dedicated computational grid (for the stall strips), according to the models developed under work package 2 of the present project [13].

2.4 Three-dimensional Aeroelastic Tool

The three-dimensional aeroelastic tool derives from the coupling of the fluid flow solver EllipSys3D together with the linear structural model to simulate the aeroelastic dynamic response of a wind turbine rotor blade.

The numerical implementation consists in using the Navier–Stokes solver to compute the flow field around the blades, and thereby the aerodynamic forces exerted on them. These forces result in the deflection of the blades, which is computed by the structural model. In turn, the structural deflection modifies the flow domain boundaries and consequently triggers a response of the flow field. This results in a so-called aeroelastic dynamic interaction.

Several schemes have been proposed for the solution in the time domain of the coupled fluid flow/structure equations that govern the aeroelastic interaction [14]. The Improved Serial Staggered procedure defined as a leap-frog scheme where the fluid subsystem is always computed at half time-stations $(\dots, t^{n-1/2}, t^{n+1/2}, t^{n+3/2}, \dots)$, while the structure subsystem is always computed at full time-stations $(\dots, t^{n-1}, t^{n}, t^{n+1}, \dots)$, is preferred. It can be summarized as follows:

1. Given the blade deflection $\mathbf{X}^n$ at time step n, and its velocity $\dot{\mathbf{X}}^n$, the structural displacement at time $t^{n+1/2}$ is predicted as:

$$\mathbf{X}^{n+1/2} = \mathbf{X}^n + \frac{\Delta t}{2}\dot{\mathbf{X}}^n$$

where the time step Δt is assumed to be the same for both the structural and the flow solver temporal integration schemes.

2. The fluid mesh is accordingly distorted to give the mesh position $\xi^{n+1/2}$ at time $n+1/2$, where ξ denotes the fluid mesh coordinates. Then the fluid subsystem is integrated in time from $t^{n-1/2}$ to $t^{n+1/2}$.

3. The fluid force field $\mathbf{F}^{n+1}$ is transferred to the structural nodes, and the corresponding flow-induced structural loads are computed.

4. The structure subsystem is integrated in time from t^n to t^{n+1}.

5. The just computed structure deflection is used as a new input for step 1.

This scheme has been shown to be second-order energy-accurate provided some few additional assumptions [15]. The deformation of the structure is taken into account into the flow solver by distorting the computational grid according to the deformation of the blades.

Note that the fluid flow and the structure discretisations are fully independent. Therefore, in Step 3 the aerodynamic forces are interpolated at specified radius stations along the blades corresponding to the force nodes of the structure discretisation. In return, in Step 2 the structural deflection of the blade is smoothened by using a spline interpolation technique between the deformation nodes before applying the grid-distortion procedure.

It must be stressed here that in the past the fluid flow solver EllipSys3D has been combined together with another, similar, structural model for both fully coupled simulations and calculation of the aerodynamic damping by means of evaluating the linear aerodynamic work, which is computed by the Navier–Stokes solver, in the same test case that is considered herein [16]. The results of the latter method are used for comparison with the ones obtained under the current work package.

2.5 Quasi-three-dimensional Aeroelastic Tool

The quasi-three-dimensional aeroelastic tool derives from the coupling of the Navier–Stokes solver of CRES with the linear elastic solver for the fully three-dimensional blade. The Navier–Stokes solver is employed at the centre nodes of each aerodynamically active element to feed the elastic solver with the aerodynamic forces at each time step. In turn, the aerodynamic surface movements, which are the elastic translations, are taken into account in the Navier–Stokes solver by solving the Navier–Stokes equations for incompressible flow in the relative frame and applying suitable inlet boundary conditions at each step, as

$$\begin{aligned} \nabla \cdot \mathbf{W} &= 0 \\ \frac{\partial \mathbf{W}}{\partial t} + \mathbf{W} \cdot \nabla \mathbf{W} - \frac{1}{Re} \nabla^2 \mathbf{W} + \frac{\nabla p}{\rho_a} + [\ddot{\mathbf{u}} + 2\boldsymbol{\Omega} \times \mathbf{W} + \boldsymbol{\Omega} \times \boldsymbol{\Omega} \times \mathbf{r}] &= 0 \end{aligned} \tag{2.4}$$

where $\mathbf{W}$ stands for the relative velocity vector related to the wind velocity vector $\mathbf{U}_\infty$, the rotational speed $\boldsymbol{\Omega}$ and the elastic displacements $\mathbf{u}$ through

$$\mathbf{W} = [\mathbf{U}_\infty + \boldsymbol{\Omega} \times \mathbf{r}] + \dot{\mathbf{u}} \tag{2.5}$$

The extra source terms in the momentum conservation equations include the acceleration due to the elastic movement, the Coriolis and the centrifugal force, owing to the transformation to the relative frame. It must be also pointed out that in the calculation of the relative velocity, no three-dimensional correction of the effective angle of attack (in the form of the blade element momentum theory, for instance) is considered; therefore the relative velocity at inlet corresponds to the geometric angle of attack without taking into account the induced flow.

Chapter 3

Definition of Test Cases

One or two blades were foreseen in the project work programme, with the first blade to be used for validation purposes and the second one for actual wind turbine rotor investigations. In the absence of aeroelastic stability experiments in the wind energy field, a thorough review was conducted in the helicopters literature in an attempt to define the validation test case. Four such experiments were reviewed covering relevant works conducted the last two decades [17, 18, 19, 20]. The search revealed, however, that no helicopter rotor stability experiment is suitable for the purposes of the project. The main reasons are listed below:

1. Most of these experiments have been conducted in hover conditions and some in forward flight conditions. Both conditions do not resemble wind turbine operation.

2. Even in these cases the available aerodynamic data are extremely limited for validation purposes (the structural data are much more complete).

3. The experiments address low angle of attack (higher Mach number also) operation, which is not of particular interest for the wind energy community.

For all these reasons it was decided to abandon the first test case and proceed directly to stability calculations of an actual wind turbine rotor. This rotor blade is based on the *LM 19.1 m* blade, which is already used in the other work packages of the present project and has been subjected to a large number of calculations in the concluded *VISCEL* project [21, 22]. The calculations are well documented in the VISCEL aerodynamic/aeroelastic database, which in turn will be enriched with the KNOW–BLADE results.

3.1 Three-dimensional Test Cases

The rotor blade used in the fully-three-dimensional and the quasi-three-dimensional aeroelastic computations corresponds to the *LM 19.1 m* blade. Its structural "beam element" data are given in [23]. For each element, its length L, its mass density $\overline{\rho}$, its mass centre coordinates $(Z_C,\ X_C)$, its polar mass moment of inertia $\overline{\rho} I_t$ with respect to the elastic centre, its bending stiffnesses with respect to $Z-$ and $X-$ axis EI_{zz} and EI_{xx}, its torsional stiffness GJ and its stiffness product EI_{xz} are provided. The mass centre coordinates are with respect to the elastic centre. Since the blade features a 1.4 m long extender, the data for the extender are also included in the same table. The pitch and cone angles are set to $0°$. The rotational speed is $\Omega = 27.1$ rpm. The air density is $\rho_a = 1.22$ kgr/m^3.

The aerodynamic characteristics of the blade, without the extender, (chord, thickness twist and aerofoil type) at different radii are also provided in [23].

Three reference sections along the span of the *LM 19.1 m* blade are defined mainly for comparison purposes. Their location along the span is included in Table 3.1.

Six test cases have been defined for wind speeds $U_\infty = 10$, 14 and 18 m/s (mandatory) and 12, 16 and 20 m/s (optional). The initial conditions correspond to an undeformed blade subjected to its aerodynamic loading. Structural damping was not considered. The test cases are summarized in Table 3.2. The runs were performed fully turbulent.

3.2 Two-dimensional, "Typical Section" Test Cases

For the two-dimensional aeroelastic calculations on a "typical section," the Section C of the *LM 19.1 m* blade (see Table 3.1) was chosen. It corresponds to a NACA 63–400 airfoil with chord $C = 0.677$ m and maximum thickness $t_{max}/C = 16$ %. The blade twist at Section C is set to zero for all two-dimensional aeroelastic calculations (the actual value for this quantity is 0.12°, which is negligible). Its linear mass is $\overline{\rho} = 39.5$ kgr/m, while the natural frequencies of the first flap and lead–lag modes are $\omega_y = 2.02$ Hz and $\omega_z = 3.23$ Hz respectively.

The aeroelastic stability on the selected "typical section" is studied for three configurations; one clean (without any accessory), one with stall strips and one with roughness tapes along the pressure and suction side. Each configuration is studied for three wind speeds, $U_\infty = 10$, 15 and 20 m/s. The stall strips are placed at the leading edge retaining geometric similarity with the so-called *P00* test case of work package 2 (see [13] for further information). The roughness tapes are placed at $x/C = 5$ % on the suction side and $x/C = 10$ % on the pressure side (see [13] for further information).

Test matrix is given in Table 3.3. The so-called 'flow angle' is the geometric angle of the relative velocity in respect to the plane of blade rotation.

Table 3.1: Definition of spanwise positions of the reference sections of the *LM 19.1 m* blade.

Section	Spanwise Position [%]	Radius [m]
A	40.98	8.40
B	71.71	14.70
C	90.73	18.60

Table 3.2: Definition of test cases for the full three-dimensional blade.

Test Case	U_∞ [m/s]	Comment
TC3D-1	10.0	Mandatory
TC3D-2	12.0	
TC3D-3	14.0	Mandatory
TC3D-4	16.0	
TC3D-5	18.0	Mandatory
TC3D-6	20.0	

Table 3.3: Definition of test cases for the two-dimensional "typical section".

Test Case	U_∞ [m/s]	Flow Angle [°]	κ	R_f	$\overline{\omega}_y$	$\overline{\omega}_z$	Accessory
TC2D-11	10.0	10.73	0.192	0.0142	4.51	7.17	Clean
TC2D-12	15.0	15.86	0.128	0.0142	4.51	7.17	Clean
TC2D-13	20.0	20.75	0.096	0.0142	4.51	7.17	Clean
TC2D-21	10.0	10.73	0.192	0.0142	4.51	7.17	Stall Strips
TC2D-22	15.0	15.86	0.128	0.0142	4.51	7.17	Stall Strips
TC2D-23	20.0	20.75	0.096	0.0142	4.51	7.17	Stall Strips
TC2D-31	10.0	10.73	0.192	0.0142	4.51	7.17	Roughness Tapes
TC2D-32	15.0	15.86	0.128	0.0142	4.51	7.17	Roughness Tapes
TC2D-33	20.0	20.75	0.096	0.0142	4.51	7.17	Roughness Tapes

Chapter 4

Aeroelastic Stability Analysis

This chapter is concerned with the aerodynamic damping results. First, the comparisons for the blade are presented, between the fully and the quasi-three-dimensional simulations, as well as for nonlinear simulations and eigenvalue analysis employing engineering-type models for the aerodynamics. Next, comparisons between the fully three-dimensional and the two-dimensional simulations are provided aiming at the assessment of the latter ones with respect to full three-dimensional computations. Then the corresponding two-dimensional simulations without aerodynamic accessories obtained by CRES and Risø are cross-compared to define a basis according to which the results for the aeroelastic behaviour in the presence of aerodynamic accessories will be judged.

4.1 Computational Details

4.1.1 CRES

Three-dimensional Blade

- 4 elements, 3 active aerodynamically;
- 66,755 grid nodes in three C–type grids consisting of 257×65, 385×65 and 385×65 nodes, which were provided by Risø;
- $k-\omega$ SST turbulence model;
- 5000 time steps with 0.001 s interval.

Two-dimensional "Typical Section"

- C–type grids consisting of 385×129, 513×129 and 385×129 nodes for the clean, the stall strip and the roughness tapes test cases, respectively, which were provided by Risø;
- $k-\omega$ SST turbulence model;
- 10000 time steps with 0.005 reduced time interval.

4.1.2 RISØ

Three-dimensional Blade

- 16 elements;

- $k-\omega$ SST turbulence model;
- 5,242,800 grid cells in 20 blocks of 64×64×64 cells;
- 6000 time steps with 0.001 s interval.

Two-dimensional "Typical Section"

- $k-\omega$ SST turbulence model;
- 31000 time steps with 0.0002 s interval.

4.2 LM 19.1 m Blade

4.2.1 Fully-three-dimensional & Quasi-three-dimensional Analysis

In Figure 4.1 the time series of the non-dimensional translations in the flapwise and the lead–lagwise direction at section C of the *LM 19.1 m* blade are presented for the mandatory test cases. In the same figure, the responses of both the fully-three-dimensional and the quasi-three-dimensional are combined for comparison purposes. Since section C is the most outboard section defined on the blade, it is expected that the translations will be maximum at this section. Therefore the stability properties extracted by these series will be representative of the stability properties of the whole blade.

From the presented distributions it is observed, that both methods produce similar results. For all wind speeds considered the translation in the flapwise direction is representative of stable behaviour; whereas the translation in the lead–lagwise direction is nearly periodic. It is also apparent that the two tools result in different steady-state responses in the flapwise direction. This is expected since in the quasi-three-dimensional tool, the three-dimensional induction effects are not modelled.

The differences in the aero-elastic behaviour are quantified in Figure 4.2, in terms of the logarithmic decrement. This quantity was extracted from the time series of Figure 4.1 by means of a moving block damping analysis method [24] and/or the modal analysis software *ME'scopeVES of Vibrant Technology Inc.* The first method employs a FFT calculation on a block of a response. The block is marched in time, and from the time evolution of the amplitude of the response at a given frequency the logarithmic damping can be calculated. Repeating this procedure for each and every time series of the translations at hand, the logarithmic decrement is obtained for the first flapwise and lead–lagwise mode for the whole wind speed range examined. It is reminded at this point that a positive value for the logarithmic decrement corresponds to stable behaviour.

The distributions of the logarithmic decrement presented in Figure 4.2 for the two modes confirm the findings reported so far; both tools predict high positive values for the flapwise mode and negative, very close to zero, values for the lead–lagwise mode indicating aeroelastic instability in the absense of structural damping. It is also observed that both tools indicate stronger instabilities as the wind speed increases; the three-dimensional one with a smaller rate though. In general the three-dimensional tool is more conservative in predicting instabilities. This can be attributed to the incapability of the quasi-three-dimensional tool to model induction effects, resulting in blade's operation at higher angles of attack.

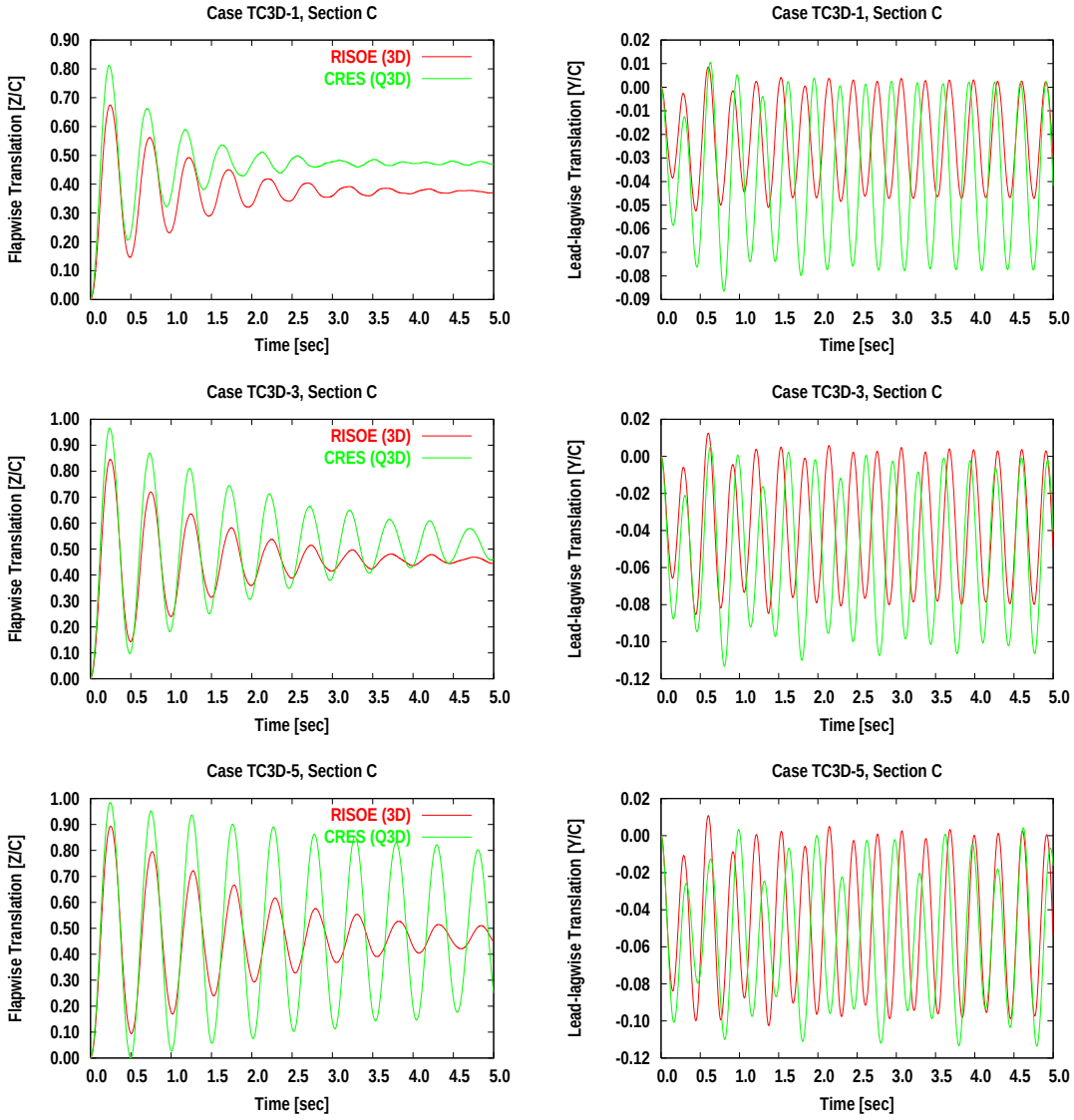

Figure 4.1: Flapwise (left) and lead–lagwise (right) translations at section C. Results from the full and the quasi three-dimensional aeroelastic tools. Top: $U_\infty = 10$ m/s, middle: $U_\infty = 14$ m/s, bottom: $U_\infty = 18$ m/s.

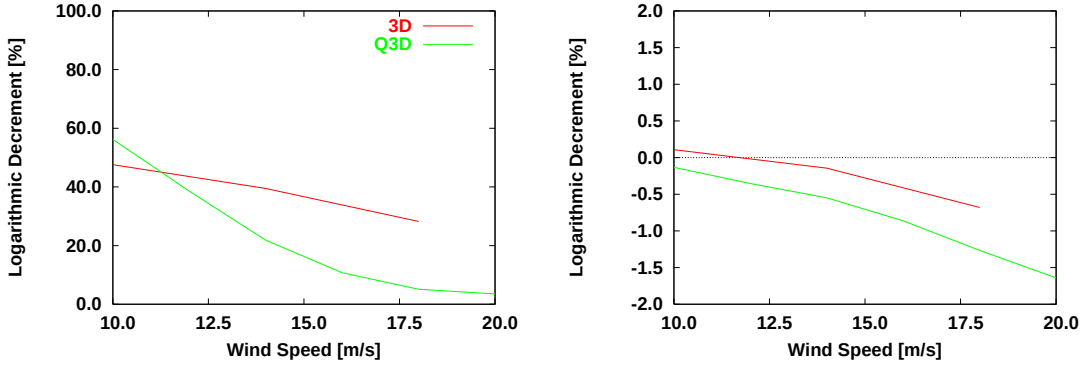

Figure 4.2: Aerodynamic damping for the first flap (left) and lead–lag (right) modes of the *LM 19.1 m* blade. Results from the full and the quasi three-dimensional aeroelastic tools.

4.2.2 Engineering Models – Eigenvalue Analyses

The information gathered from the fully three-dimensional and the quasi-three-dimensional tools is also valuable for the assessment of the, very popular in aeroelastic applications, engineering-type aerodynamic models. Such models are used not only by the partners involved in this work package (Risø usually employs the Beddoes–Leishman [25] model, while CRES uses the Extended Onera Lift and Drag [26]) but also by other organizations (ECN has developed such a dynamic stall model [27]) very often. They are very popular because they are suitable for calculations in beam element type structural models when combined with the blade element momentum (BEM) theory, relatively simple in formulation and not very time consuming, especially when compared with a Navier–Stokes treatment of the flow around a blade (even a two-dimensional).

To this end, the same structural model that was involved in the quasi-three-dimensional tool is introduced in a stability tool for wind turbine blades [11] and nonlinear integration of the equations of motion in time was carried out. The necessary aerodynamic profile coefficients (C_L and C_D) were extracted from three-dimensional Navier–Stokes computations of the flow around the blade for wind speeds 7, 10, 12, 13, 15 and 17 m/s using a transitional turbulent model [28]. The equivalent angle of attack has been approximated by means of determining the reduced axial valocity in the rotor plane [28]. Since the polars have been extracted by three-dimensional computations, the tip loss is included and there is no need to include it in the BEM method. On the other hand, the range of the angles of attack covered does not cover the range needed for the simulations reported herein. So, as depicted from Figure 4.3 the original profile coefficients were smoothed and extrapolated to cover a wider range of angles of attack. Evidently, this introduces some error in the stability calculations performed herein. Nevertheless as a low level a priori check, the smoothed/extrapolated profile coefficients have been used in predicting the power curve for the *NORDTANK 500/41* wind turbine that is equipped with *LM 19.1 m* blades. The agreement with the measured curve is very good, only a slight overestimation is reported, as depicted from Figure 4.4, where the power and thrust curves for the *NORDTANK 500/41* wind turbine are presented.

Apart from the simulations in the time domain using an engineering-type unsteady aerodynamic model [26], two linear, eigenvalue-type analyses have been performed employing both quasi-steady and unsteady aerodynamic modelling (for the latter the same engineering-type model is used). For the sake of consistency, eigenvalue analysis and simulations in the time domain share identical input (aerodynamic and structural). Finally, results from the combination of a structural finite beam element model with a three-dimensional Navier–Stokes solver in an uncoupled manner are considered [16]. In this method, the modal aerodynamic damping is evaluated by computing the aerodynamic forces upon a prescribed eigenmode deformation of the structure, which has been determined in advance by a structural modal analysis.

In Figure 4.5 the lift coefficient loops at section C of the blade are presented for six wind speeds, as obtained by the quasi-three-dimensional aeroelastic tool. As the wind speed increases, the blade operates at post-stall conditions (higher angles of attack). In this region, the advanced aeroelastic tools suffer the limitation of the turbulent model in use to cover sufficiently separation. On the other hand, the polars introduced in the engineering-type models exhibit the aforementioned uncertainty in the post-stall regime.

In Figure 4.6 the same with Figure 4.1 non-dimensional translations in the flapwise and the lead–lagwise direction at section C are presented. In the figure, the corresponding responses by the nonlinear analysis in the time domain using the engineering-type aerodynamic model have been included. In Figure 4.7 the logarithmic decrement distributions for the two modes are presented, as obtained by the two three-dimensional tools (fully and quasi), the nonlinear

analysis in the time domain with the unsteady aerodynamic model, the two eigenvalue-type analyses and the prescribed motion method.

In the time series of the translations in the flapwise direction for the engineering-type aerodynamic model, a high frequency oscillation is observed for the higher wind speeds. It can be attributed to the poor aerodynamic input for the post stall regime that was filled in by extrapolating the profile coefficients. The distributions for the flapwise translations show qualitative similarity (decaying responses with decreasing rate with the increase in wind speed) for all tools. On the contrary, the lead–lagwise response of the engineering-type unsteady model is clearly not stable, whilst all other tools predict a nearly periodic response.

These features are reflected in the logarithmic decrement distributions too. All methods predict the decrease in aerodynamic damping with the increase of wind speeds for the flapwise mode, and a minimum value above 15 m/s is observed. Both eigenvalue analyses produce qualitatively similar results with the advanced aeroelastic tools, the only difference being that the distributions are steeper for the flapwise mode and in a quasi-steady aerodynamic approximation negative values also appear. A good agreement is also observed in the distributions of the aerodynamic damping for the lead–lagwise mode with all methods predicting a decrease of damping with the increase of wind speed. In this case, negative values appear for the whole range of wind speeds. Again, the results of the eigenvalue analyses correspond to larger instabilities, in conformity to the time series of the response at the same direction.

In perspective, the uncoupled method (where there is no aerodynamic and structural interaction) results in higher values of aerodynamic damping compared to the three-dimensional aeroelastic tool. The quasi-three-dimensional tool results in lower aerodynamic damping values in the higher wind speeds and higher damping values in the lower wind speed regime.

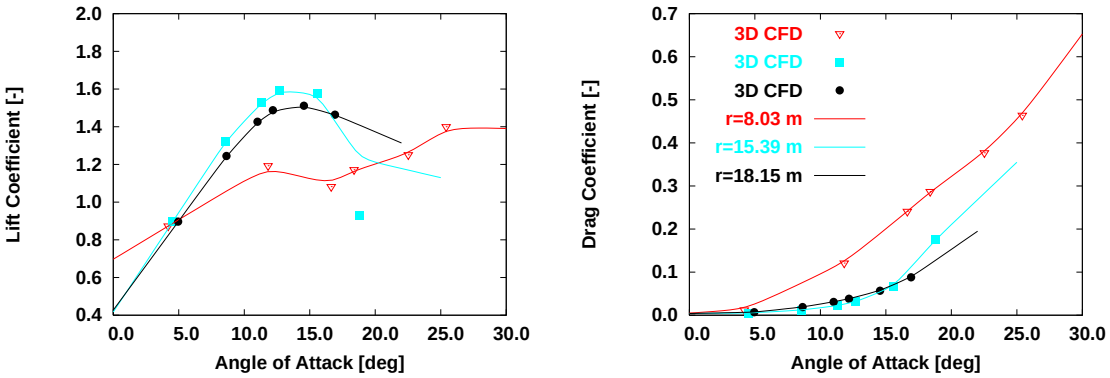

Figure 4.3: Aerodynamic profile coefficients for sections A, B and C of the *LM 19.1 m* blade. Symbols: 3D CFD computations [28], lines: curve fitting by CRES.

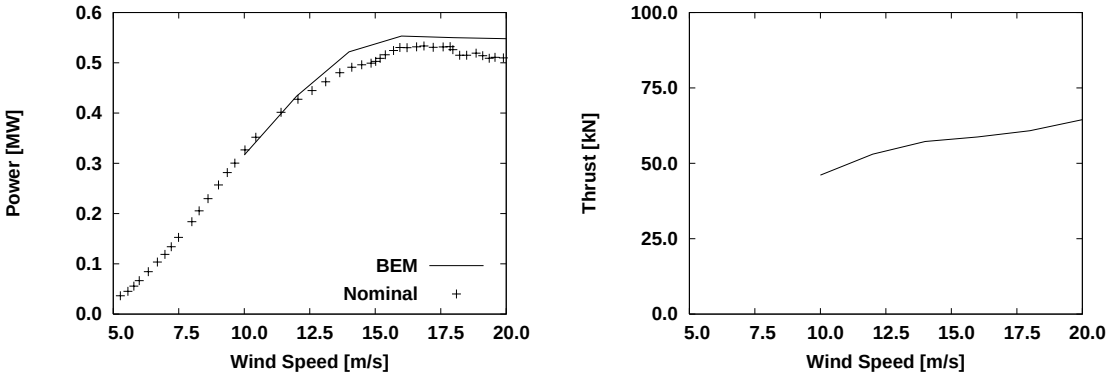

Figure 4.4: Power (left) and thrust (right) curves for the *LM 19.1 m* blade.

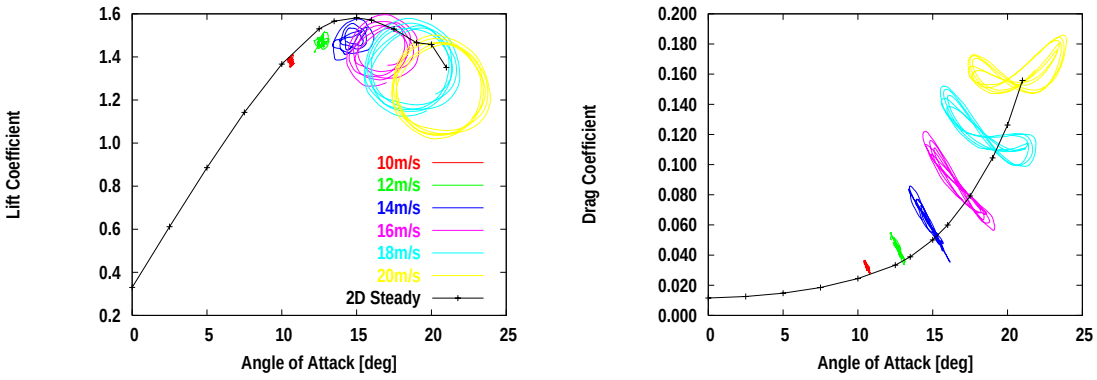

Figure 4.5: Lift (left) and drag (right) coefficient loops at section C of the *LM 19.1 m* blade for different wind speeds as obtained by the quasi-three-dimensional aeroelastic tool.

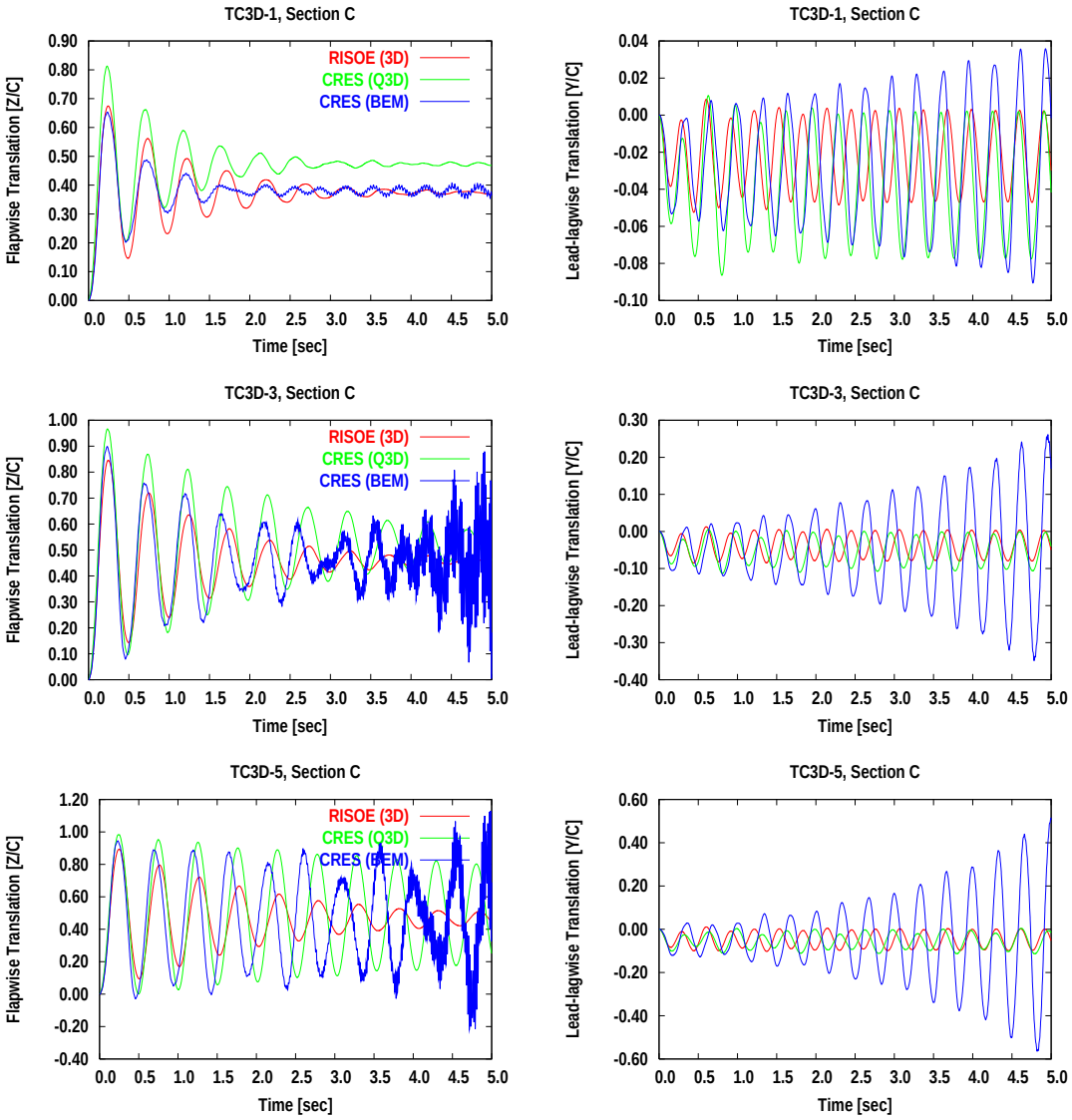

Figure 4.6: Flapwise (left) and lead–lagwise (right) translations at section C. Results from the advanced aeroelastic tools and a BEM method. Top: $U_\infty = 10$ m/s, middle: $U_\infty = 14$ m/s, bottom: $U_\infty = 18$ m/s.

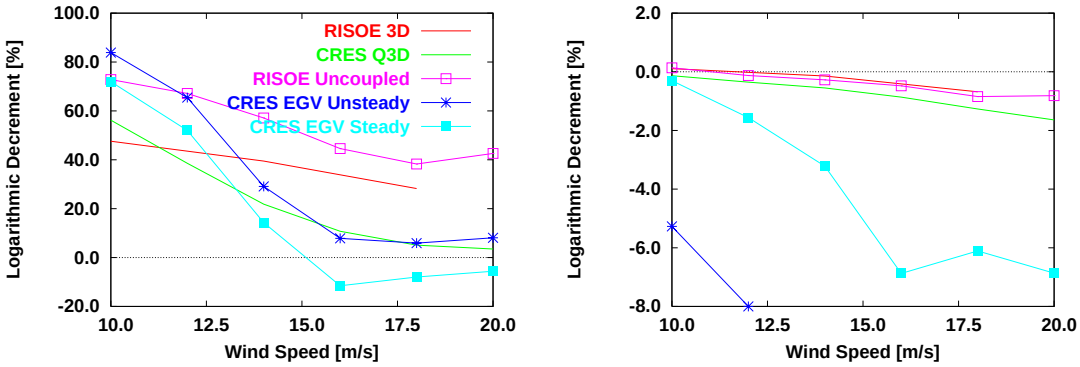

Figure 4.7: Aerodynamic damping for the first flap (left) and lead–lag (right) modes of the *LM 19.1 m* blade. Results from the advanced aeroelastic tools, a BEM method, two linear eigenvalue analyses and an uncoupled linear method.

4.3 "Typical Section"

4.3.1 Fully-three-dimensional & "Typical Section" Analysis

In Figure 4.8 the time series of the translations in the flapwise and the lead–lagwise directions are presented at section C of the *LM 19.1 m* blade. The time series presented have been obtained by the fully-three-dimensional and the two-dimensional aeroelastic tools by Risø; the latter combined with the two-dimensional counterpart of EllipSys3D. From the computational point of view differences between the two approaches are restricted in the the selection of the time step and the quality of the mesh that obviously affect the CFD method. On the other hand from the modelling point of view, the two-dimensional aeroelastic tool cannot cover three-dimensional flow effects. In addition, since it is not combined with any actuator disk method, the induced flow is not modelled and the angles of attack that the blade section experiences are in turn higher for the same wind speed, when compared to the fully-three-dimensional. It is also noted that in Figure 4.8 there is an inconsistency for the wind speeds in the two graphs of the middle row of the figure; the three-dimensional corresponds to 14 m/s, while the two-dimensional to 15 m/s. It is revealed as difference in the damped frequency of the obtained translations. There is qualitative agreement between the three-dimensional and the two-dimensional translations; all responses in the flapwise direction are decaying oscillations while the ones in the lead–lagwise direction are nearly periodic for both tools.

In Figure 4.9 the logarithmic decrements that correspond to these translations are plotted. From the comparison of the logarithmic decrements distributions by the two tools, the findings observed in the translation responses are verified; they both result in high positive values for the flapwise mode and near zero or negative values for the lead–lagwise mode. A decrease in damping with the increase in wind speed is also observed (with the exception of 20 m/s for the two-dimensional tool). The three-dimensional tool is more conservative in predicting instabilities for the lead–lag mode and more monotonous for the flap mode. It seems that the three-dimensional effects 'stabilize' the flow.

4.3.2 Clean "Typical Section"

In Figure 4.10 the evolution in time of the translations in the flapwise and the lead–lagwise directions at section C of the *LM 19.1 m* blade are presented. The time series presented have been obtained by the aeroelastic tools for the "typical section" by Risø and CRES. Since the grids used by CRES have been provided by Risø, the differences between the two predictions are restricted in the selection of the time step and the differencing schemes in the CFD methods and the aeroelastic coupling scheme. In Figure 4.11 the logarithmic decrements corresponding to these translations are plotted. For the flap mode, both tools result in high positive values of aerodynamic damping, agreement is better in the lower wind speed (when the section operates in the linear regime of the lift coefficient polar) which deteriorates as the wind speed increases. For this mode, results by the CRES tool are monotonous (decreasing aerodynamic damping with increasing wind speed), while the ones by the Risø tool present a minimum value at 15 m/s, as already mentioned. As a result of the aforementioned differences, in the higher wind speed even different steady-state responses are obtained. In the lead–lag mode, the tools behave differently, with the CRES tool resulting in stable responses (of very low decaying rate though) whilst the Risø tool in nearly periodic with small negative logarithmic decrement values. For both modes examined, the Risø tool results in lower aerodynamic damping values than the CRES tool.

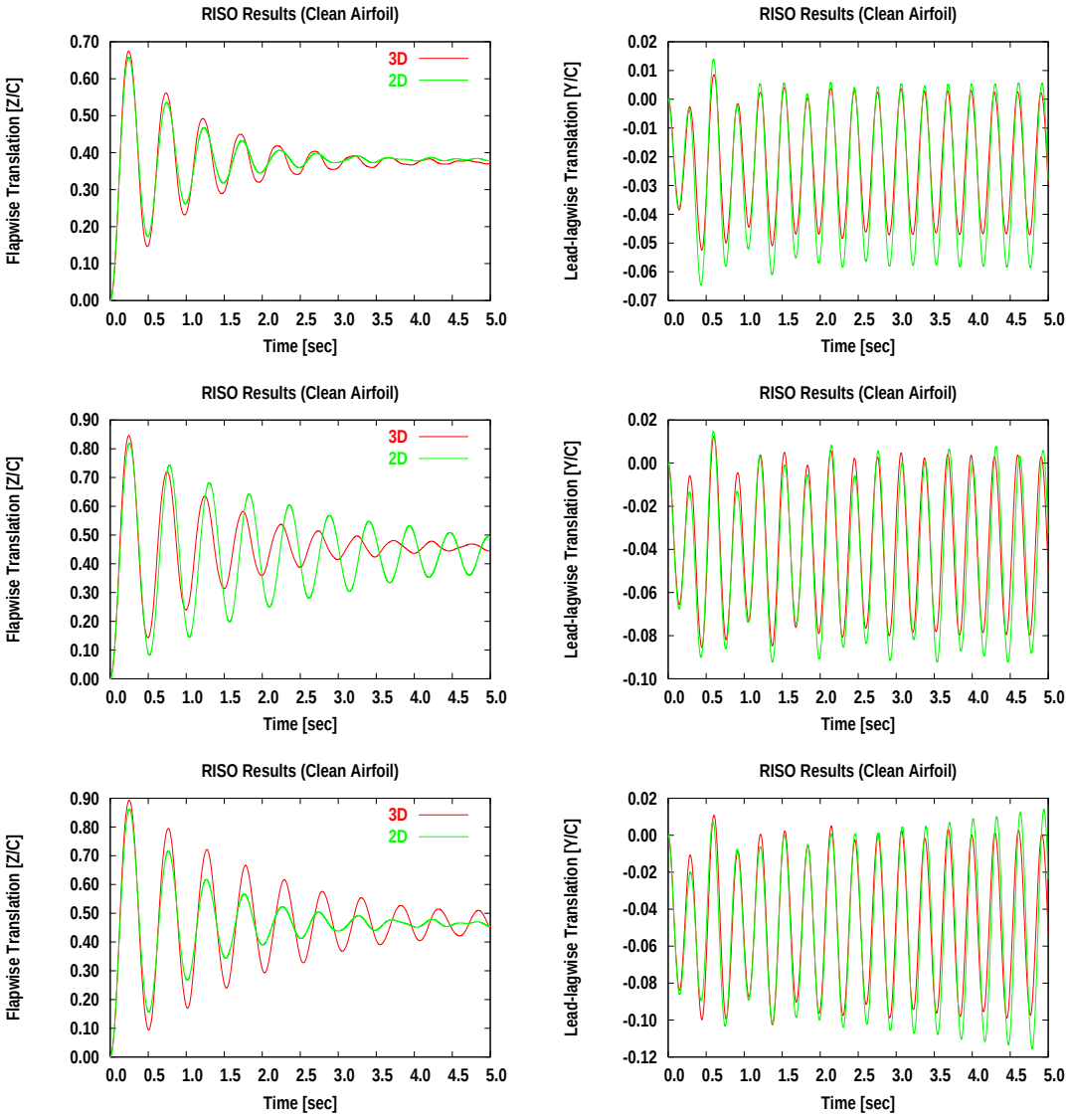

Figure 4.8: Flapwise (left) and lead–lagwise (right) translations at section C. Results from the three- and the two-dimensional aeroelastic tools by Risø. Top: $U_\infty = 10$ m/s, middle: $U_\infty = 14$ m/s (3D) and 15 m/s (2D), bottom: $U_\infty = 20$ m/s.

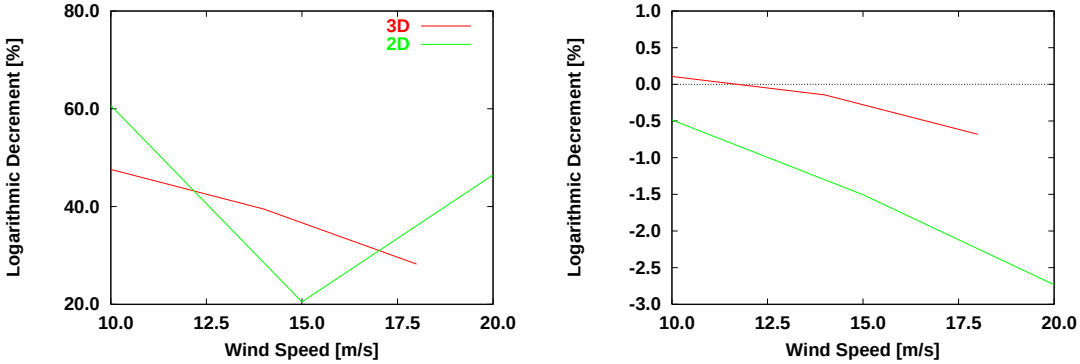

Figure 4.9: Aerodynamic damping for the first flap (left) and lead–lag (right) modes of the *LM 19.1 m* blade. Results from the three- and the two-dimensional aeroelastic tools by Risø.

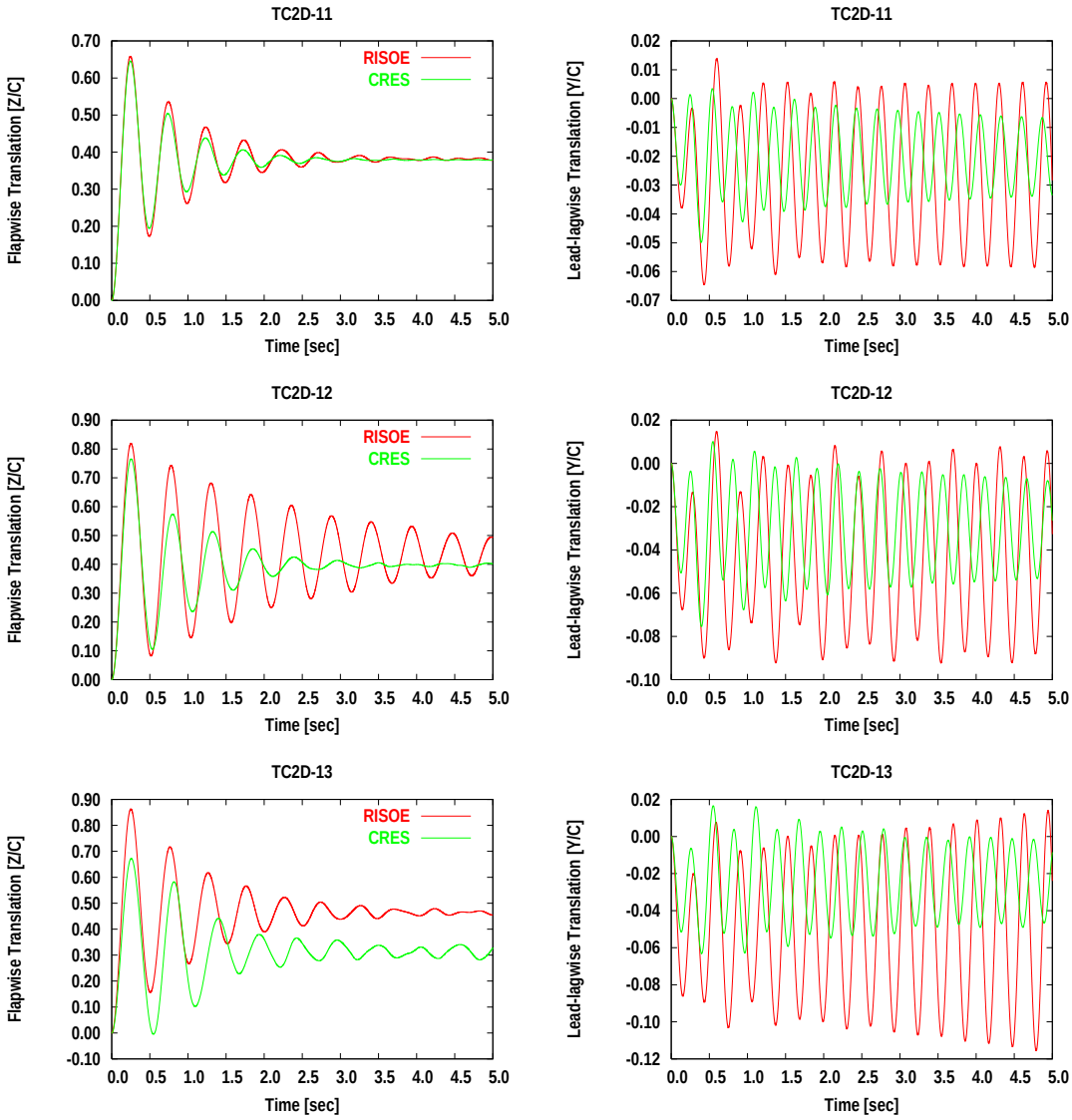

Figure 4.10: Flapwise (left) and lead–lagwise (right) translations at section C. Results from the two-dimensional aeroelastic tools by Risø and CRES. Top: $U_\infty = 10$ m/s, middle: $U_\infty = 15$ m/s, bottom: $U_\infty = 20$ m/s.

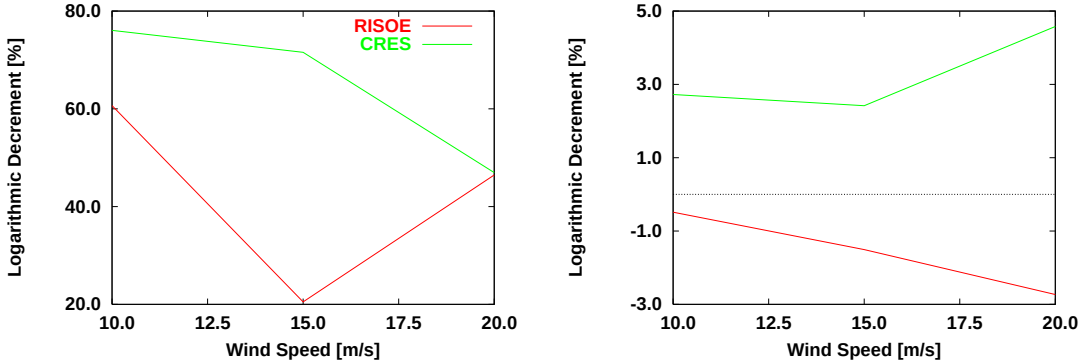

Figure 4.11: Aerodynamic damping for the first flap (left) and lead–lag (right) modes of the *LM 19.1 m* blade. Results from the two-dimensional aeroelastic tools by Risø and CRES.

4.4 "Typical Section" Equipped with Aerodynamic Accessories

In Figures 4.12 and 4.14 the evolution in time of the translations in the flapwise and the lead–lagwise directions at section C of the *LM 19.1 m* blade are presented for blades equipped with stall strips and roughness tapes by the Risø and the CRES tool, respectively. For the sake of comparison, the corresponding responses for the clean configuration are included. The corresponding aerodynamic damping distributions are presented in Figures 4.13 and 4.15 for the Risø and the CRES tool, respectively.

From the comparison of both the translations and the aerodynamic damping distributions by the two tools for the clean and the roughness tapes configurations, very small differences are observed for both modes considered. The differences in the responses are bigger in the higher wind speed, but even in this case the differences in logarithmic decrement are much smaller, nearly negligible. So, in the presence of roughness tapes, the differences in the responses and the aerodynamic damping values by the two tools reflect the differences observed in the corresponding distributions for the clean configuration (see Figure 4.16 and 4.11).

On the other hand, the responses obtained by both tools in the presence of stall strips are considerably different from the corresponding responses for the clean configuration and the roughness tapes. So, it appears that the stall strips influence the aeroelastic stability of the "typical section". By examining the distributions of the aerodynamic damping predicted by the two tools, it is observed that both tools predict lower damping values for the stall strips configurations compared to the clean configuration, even at the higher wind speeds. This behaviour is opposed to the expectations; as stall strips enhance stability in the penalty of reduced power and this is the main reason for their application in wind turbine blades. The inability of both tools to capture the correct physical trend in the stall strips cases is closely connected to the inability of the adopted, computational, model for stall strips to successfully predict the corresponding test cases under work package 2 of this project [13]. Apart from this disagreement with reality, differences appear also between the two tool predictions (see Figure 4.17). They are severe in the lower wind speeds, where there is no agreement if the behaviour is stable or not for both modes (when a stable response is obtained by one tool, an unstable one is given by the other). On the contrary, for wind speeds above 15 m/s both tools result to similar aerodynamic damping values.

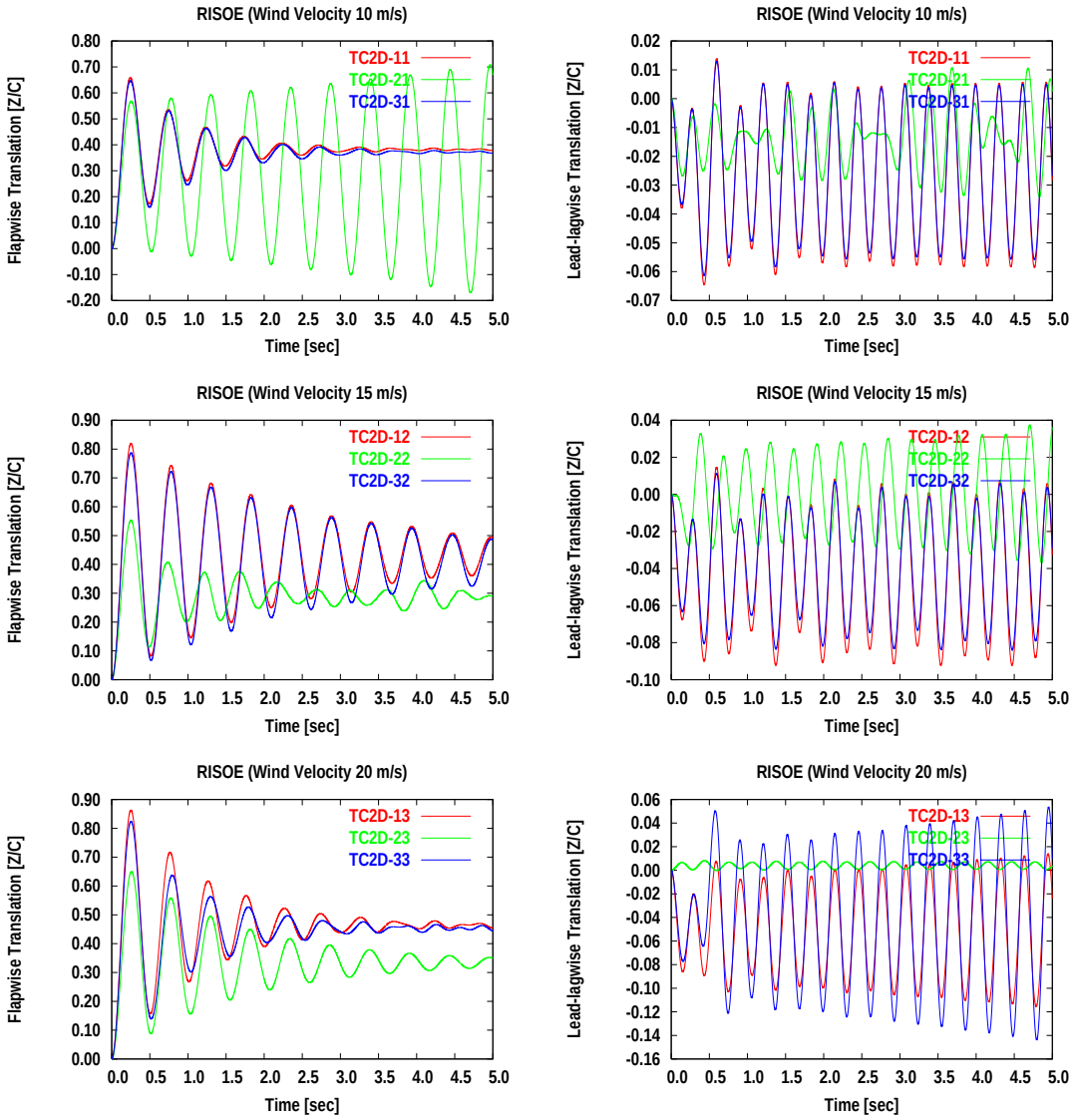

Figure 4.12: Flapwise (left) and lead–lagwise (right) translations at section C with and without aerodynamic accessories. Results from the two-dimensional aeroelastic tool by Risø. Top: $U_\infty = 10$ m/s, middle: $U_\infty = 15$ m/s, bottom: $U_\infty = 20$ m/s.

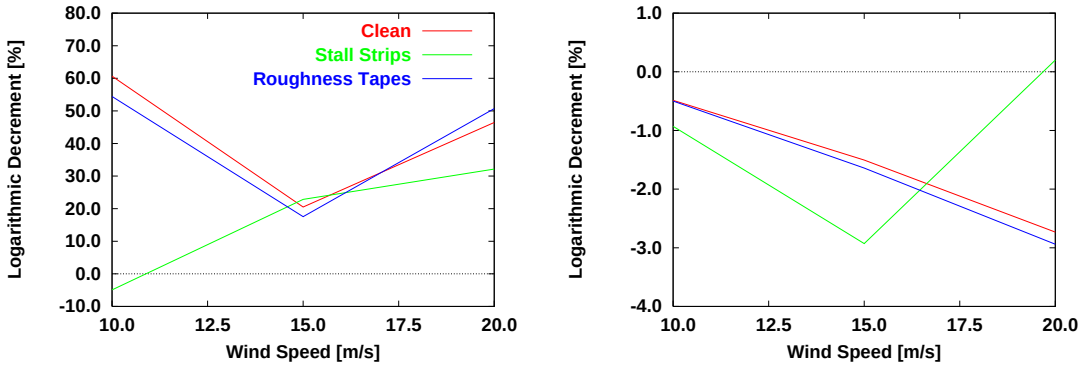

Figure 4.13: Aerodynamic damping for the first flap (left) and lead–lag (right) modes of the *LM 19.1 m* blade with and without aerodynamic accessories. Results from the two-dimensional aeroelastic tool by Risø.

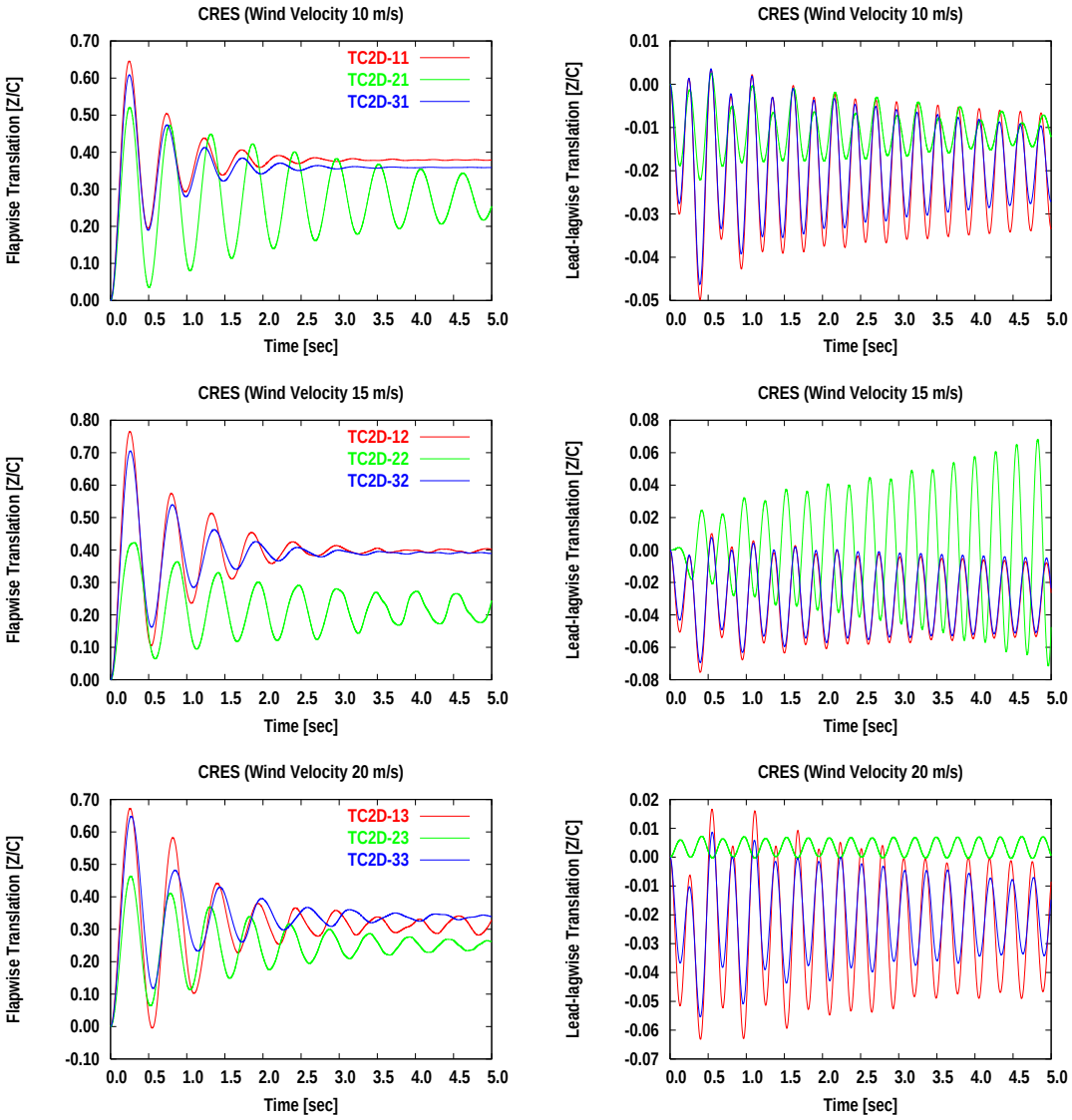

Figure 4.14: Flapwise (left) and lead–lagwise (right) translations at section C with and without aerodynamic accessories. Results from the two-dimensional aeroelastic tool by CRES. Top: $U_\infty = 10$ m/s, middle: $U_\infty = 15$ m/s, bottom: $U_\infty = 20$ m/s.

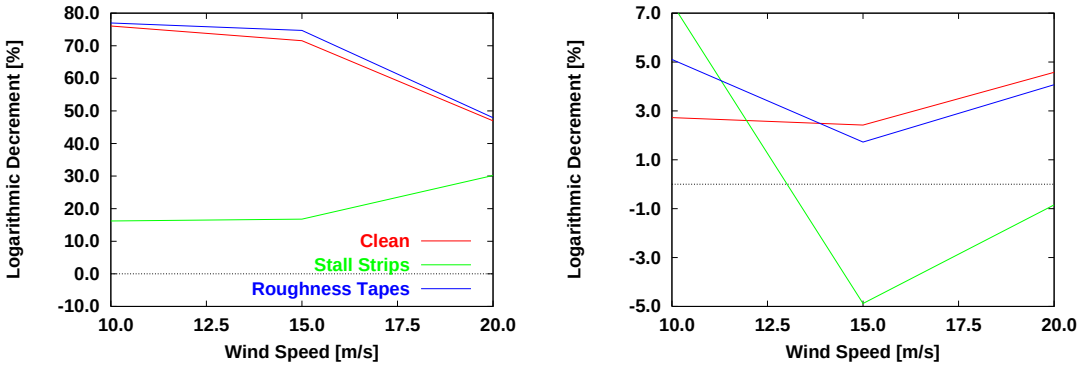

Figure 4.15: Aerodynamic damping for the first flap (left) and lead–lag (right) modes of the *LM 19.1 m* blade with and without aerodynamic accessories. Results from the two-dimensional aeroelastic tool by CRES.

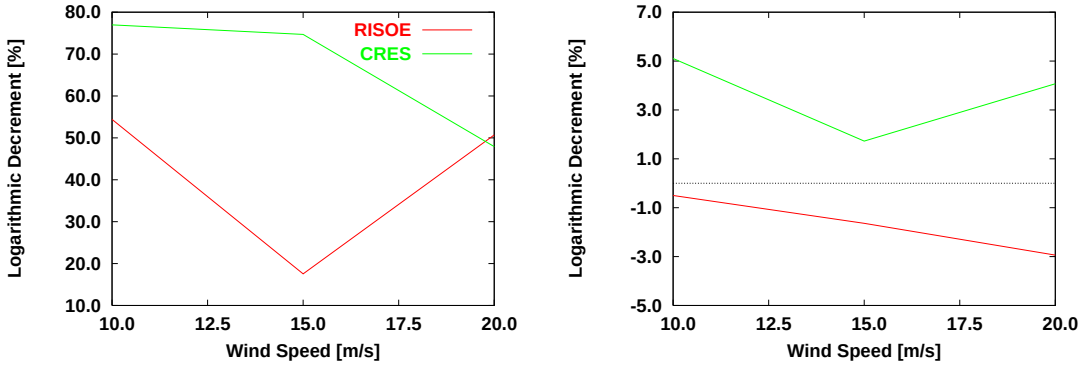

Figure 4.16: Aerodynamic damping for the first flap (left) and lead–lag (right) modes of the *LM 19.1 m* blade in the presence of roughness tapes.

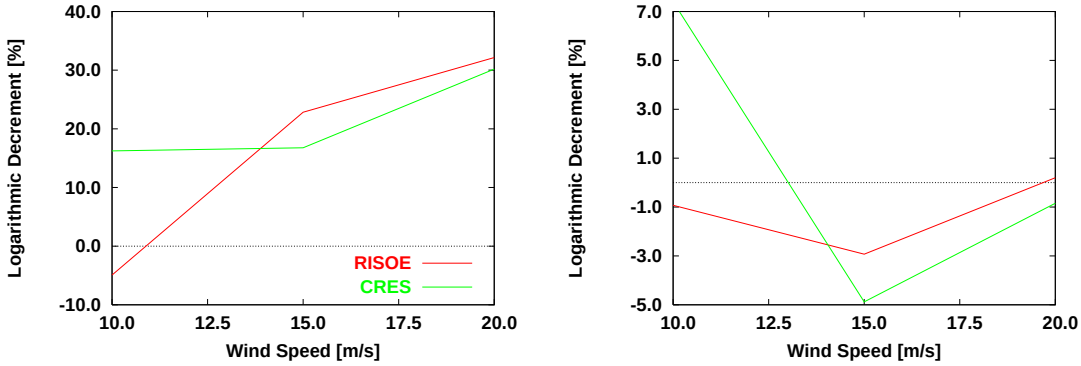

Figure 4.17: Aerodynamic damping for the first flap (left) and lead–lag (right) modes of the *LM 19.1 m* blade in the presence of stall strips.

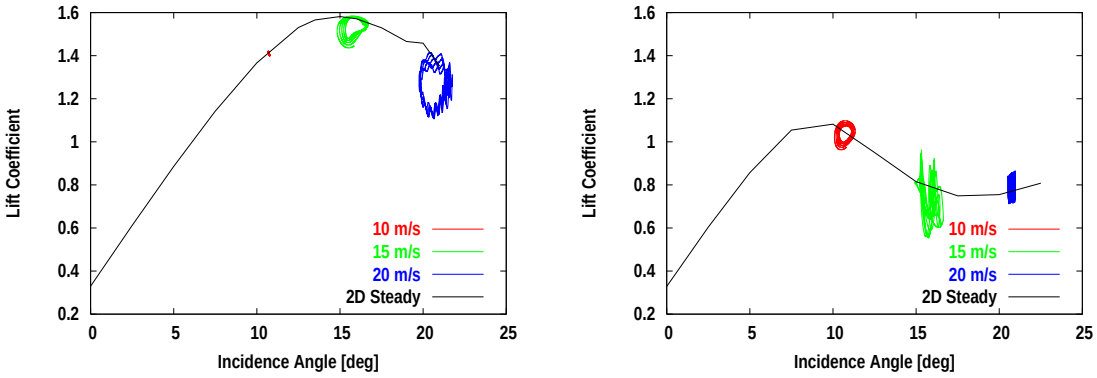

Figure 4.18: Lift coefficient loops at section C for different wind speeds with (right) and without stall strips.

Chapter 5

Conclusions

The problem of the aeroelastic stability of wind turbine blades is addressed in this report by advancing the aerodynamic modelling in the beam element type codes from the engineering-type empirical models (as the Onera or the Beddoes–Leishman) to unsteady, two- or three-dimensional, Navier–Stokes solvers. The state-of-the-art in aerodynamic modelling in beam element type codes before the present project was connected to the use of engineering-type aerodynamic models, while the user of Navier–Stokes solvers was restricted only in a two-dimensional basis, to aeroelastic tools developed for the so-called "typical section". In this project, structural models for the full wind turbine blade have been combined with two-dimensional and three-dimensional unsteady Navier–Stokes solvers. The relative disadvantage of the quasi-three-dimensional approach (where the elastic solver is coupled with a two-dimensional Navier–Stokes solver) is its inability to model induced flow. The luck of a validation test case did not allow for quantitative comparisons with experimental data to be carried out; instead the results of the advanced aeroelastic tools are qualitatively cross-compared.

An evaluation of the existing engineering-type aerodynamic model is also attempted by comparing the aerodynamic damping of the two advanced aeroelastic tools with the aerodynamic damping results of the nonlinear analysis in the time domain with an unsteady aerodynamic model, the aerodynamic damping of two linear, eigenvalue-type analyses and an uncoupled method, where the modal aerodynamic damping is evaluated by computing the aerodynamic forces upon a prescribed eigenmode deformation of the structure, which has been determined in advance by a structural modal analysis. All approaches (eigenvalue or time integration of the equations of motion) but the ones that use a Navier–Stokes type aerodynamic modelling are in need of very well defined aerodynamic input (lift, drag and moment coefficients). Obtaining complete lift and drag distributions for the whole range of wind speeds covered in this report for the wind turbine blade was not possible, and therefore only a qualitative comparison between engineering-type models and the advanced aeroelastic codes was attempted.

All methods predicted qualitatively similar results. They all resulted in positive aerodynamic damping values for the flap mode, in a decrease in damping with the increase of wind speeds and in a minimum value for the damping for wind speed around 15 m/s. The eigenvalue analyses resulted in steeper distributions for this mode. In a quasi-steady aerodynamic approximation negative values also appeared. The agreement in aerodynamic damping decrease with the increase of wind speed is also observed in the distributions for the lead–lag mode. In this case, negative values appear for the whole range of wind speeds examined. Again, the results of the eigenvalue analyses correspond to larger instabilities. In perspective, the uncoupled, linear method results in higher values of aerodynamic damping compared to the three-dimensional aeroelastic tool. The quasi-three-dimensional tool results in lower aero-

dynamic damping values in the higher wind speeds and in lower damping values in the lower wind speed regime.

Apart from the computations for the full blade, two-dimensional computations for the so-called "typical section" have been carried out. The innovative feature of these computations lies in the fact that their comparison to their three-dimensional counterpart allows for conclusions to be drawn regarding the ability of two-dimensional tools to provide reliable estimations of the damping characteristics of a blade, as well as the investigation of the damping characteristics for blades equipped with roughness tapes and stall strips. The two-dimensional aeroelastic tools resulted in similar aerodynamic damping values (positive for the flap and zero or negative for higher wind speeds for the lead–lag mode). Qualitative agreement was better for the lead–lag mode. The presence of roughness tapes has a small, rather negligible impact on aeroelastic stability as depicted by the results of both aeroelastic tools. On the other hand, in conformity to the inability of the adopted computational model to successfully predict the corresponding test cases under work package 2 of the project [13], the aeroelastic tools are not capable to predict the correct physical trends when the blade is equipped with stall strips. The resulting decrease in damping in the computations by both tools is not in accordance with experience.

Bibliography

[1] Michelsen, J. A., (1992), Basis3D – A Platform for Development of Multiblock PDE Solvers, Technical Report No. AFM 92-05, Technical University of Denmark.

[2] Michelsen, J. A., (1994), Block Structured Multigrid Solution of 2D and 3D Elliptic PDE's, Technical Report No. AFM 94-06, Technical University of Denmark.

[3] Sørensen, N. N., (1995), General Purpose Flow Solver Applied to Flow over Hills, Technical Report Risø–R–827(EN), Risø National Laboratory, Roskilde, Denmark.

[4] Rhie, C. M., and Chow, W. L., (1983), "Numerical Study of the Turbulent Flow Past an Airfoil with Trailing Edge Separation," *J. AIAA*, **21**, pp. 1525–1532.

[5] Issa, R. I., (1986), "Solution of Implicitly Discretized Fluid Flow Equations by Operator Splitting," *J. Computational Physics*, **62**, pp. 40–65.

[6] Yeo, R. W., Wood, P. E., and Hrymak, A. N., (1991), "A Numerical Study of Laminar 90–Degree Bend Duct Flow with Different Discretization Schemes," *ASME J. Fluids Engineering*, **113**, pp. 563–568.

[7] Menter, F. R., (1993), "Zonal Two–Equation Turbulence Models for Aerodynamic Flows," AIAA No. Paper 93–2906.

[8] Donea, J., (1982), "An Arbitrary Lagrangian–Eulerian Finite Element Method for Transient Fluid–Structure Interactions," *Comput. Methods Appl. Mech. Eng.*, **33**, pp. 689–723.

[9] Ferziger, J. H., and Perić, M., (1996), *Computational Methods for Fluid Mechanics,* Springer–Verlag.

[10] Patankar, S. V., and Spalding, D. B., (1972), "A Calculation Procedure for Heat, Mass, and Momentum Transfer in Three–Dimensional Parabolic Flows," *Int. J Heat & Mass Transfer*, **15**, pp. 1787–1806.

[11] Chaviaropoulos, P. K., (2001), "Flap/Lead–Lag Aeroelastic Stability of Wind Turbine Blades," *J. Wind Energy*, **4**:4, pp. 183–200.

[12] Chaviaropoulos, P. K., (1999), "Flap/Lead–Lag Aeroelastic Stability of Wind Turbine Blade Sections," *J. Wind Energy*, **2**:2, pp. 99–112.

[13] Johansen, J., Sørensen, N. N., Zahle, F., Kang, S., Nikolaou, I., Politis, E. S., Chaviaropoulos, P. K., and Ekaterinaris, J., (2004), KNOW–BLADE Task–2 Report; Aerodynamic Accessories, Technical Report Risø–R–1482(EN), Risø National Laboratory, Roskilde, Denmark.

[14] Farhat, C., Koobus, B., and Lesoinne, M., (1996), "High Fidelity and High Performance Computational Methodology for the Solution of Viscous Aeroelastic Response Problems," *Proc. First AFOSR Conference on Dynamic Motion CFD*, Rutgers University, NJ, 3–5 June, pp.159–187.

[15] Piperno, S., and Farhat, C., (2001), "Partitioned Procedures for the Transient Solution of Coupled Aeroelastic Problems - Part II: Energy Transfer Analysis and Three-Dimensional Applications," *Comput. Methods Appl. Mech. Eng.*, **190**, pp. 3147–3170.

[16] Bertagnolio, F., Sørensen, N., Hansen, M., and Mac Gaunaa, (2003), "Aeroelastic Simulation of a Wind Turbine Airfoil by Coupling CFD and a Beam Element Model," *Proc. 2003 European Wind Energy Conference & Exhibition*, Madrid, Spain, June 16–19.

[17] Bousman, W. G., (1981), "An Experimental Investigation of the Effects of Aeroelastic Couplings on Aeromechanical Stability of a Hingeless Rotor Helicopter," *J. American Helicopter Society*, **26**:1, pp. 46–54.

[18] McNulty, M. J., (1989), Flap–Lag Stability Data for a Small–Scale Isolated Hingeless Rotor in Forward Flight, Technical Report NASA–TM–102189, Ames Research Center, Moffett Field, CA.

[19] Maier, T. H., Sharpe, D. L., and Lim, J. W., (1995), "Fundamental Investigation of Hingeless Rotor Aeroelastic Stability, Test Data and Correlation," *Proc. American Helicopter Society 51st Annual Forum*, Forth Worth, TX, pp. 1176–119.

[20] Ormiston, R. A., and Bousman, W. G., (1975), "A Study of Stall Induced Flap–Lag Instability of Hingeless Rotors," *J. American Helicopter Society*, **29**:1, pp. 20–30.

[21] Chaviaropoulos, P. K., Nikolaou, I. G., Aggelis, K. A., Sørensen, N. N., Johansen, J., Hansen, M. O. L., Mac Gaunaa, Hambraus, T., von Geyr, Heiko Frhr., Hirsch, Ch., Kang, S., Voutsinas, S. G., Tzabiras, G., Perivolaris, Y., and Dyrmose, S. Z., (2003), "Viscous and Aeroelastic Effects on Wind Turbine Blades. The VISCEL project. Part I: 3D Navier-Stokes Rotor Simulations," *J. Wind Energy*, **6**:4, pp. 365–385.

[22] Chaviaropoulos, P. K., Sørensen, N. N., Hansen, M. O. L., Nikolaou, I. G., Aggelis, K. A., Johansen, J., Mac Gaunaa, Hambraus, T., von Geyr, Heiko Frhr., Hirsch, Ch., Kang, S., Voutsinas, S. G., Tzabiras, G., Perivolaris, Y., and Dyrmose, S. Z., (2003), "Viscous and Aeroelastic Effects on Wind Turbine Blades. The VISCEL Project. Part II: Aeroelastic Stability Investigations," *J. Wind Energy*, **6**:4, pp. 387–403.

[23] Politis, E. S., and Chaviaropoulos, P. K., (2002), Work Package 4: Test Case Definition, Technical Report on KNOW–BLADE Project, Centre for Renewable Energy Sources, August 2002.

[24] Smith, C. B., and Werely, N. M., (1996), "Transient Analysis for Damping Identification in Rotating Composite Beams with Integral Damping Layers," *Smart Material Structures*, **5**, pp. 540–550.

[25] Hansen, M. H., Gaunaa, M., and Madsen, H. Aa., (2003), A Beddoes-Leishman Type Dynamic Stall Model in State-Space and Indicial Formulations, Technical Report Risø–R–1354(EN), Risø National Laboratory.

[26] Petot, D., (1989), "Differential Equation Modelling of Dynamic Stall," *Recherche Aerospatiale*, **5**, pp. 59–72.

[27] Snel, H., (1997), "Dynamic Stall Modelling: Some Results," *Proc. Eleventh IEA Symposium on Wind Turbine Aerodynamics*, Netherlands Energy Research Foundation ECN, Petten, The Netherlands.

[28] Johansen, J., and Sørensen, N. N., (2004), "Aerofoil Characteristics from 3D CFD Rotor Computations," *J. Wind Energy*, **7**:4, pp. 283–294.

Mission

To promote an innovative and environmentally sustainable technological development within the areas of energy, industrial technology and bioproduction through research, innovation and advisory services.

Vision

Risø's research **shall extend the boundaries** for the understanding of nature's processes and interactions right down to the molecular nanoscale.

The results obtained shall **set new trends** for the development of sustainable technologies within the fields of energy, industrial technology and biotechnology.

The efforts made **shall benefit** Danish society and lead to the development of new multi-billion industries.